Cement and Concrete Research 39 (2009) 1217–1229

Contents lists available at ScienceDirect

Cement and Concrete Research

journal homepage: http://ees.elsevier.com/CEMCON/default.asp

Multiple cracking and strain hardening in fiber-reinforced concrete under uniaxial tension

Alessandro P. Fantilli [a,*], Hirozo Mihashi [b,1], Paolo Vallini [a,2]

[a] Department of Structural and Geotechnical Engineering, Politecnico di Torino, Corso Duca degli Abruzzi 24, 10129 Torino, Italy
[b] Department of Architecture and Building Science, School of Engineering, Tohoku University, Aramaki Aoba 6-6-11-1209, Aoba-ku, Sendai 980-8579, Japan

ARTICLE INFO

Article history:
Received 12 September 2008
Accepted 19 August 2009

Keywords:
C: Bond properties
C:Tensile properties
E: Fiber reinforcement
E: High Performance Concrete
E: Modelling

ABSTRACT

Fiber-reinforced concrete (FRC) showing strain hardening after cracking is commonly defined as High Performance Fiber-Reinforced Cementitious Composite (HPFRCC). In the post-cracking stage, several cracks develop before complete failure, which occurs when tensile strains localize in one of the formed cracks. As is well known, multiple cracking and strain hardening can be achieved in cement-based specimens subjected to uniaxial tension by increasing the volume fraction of steel fibers with hooked ends, or by using plastic fibers with and without steel fibers, or by means of high bond steel fibers (e.g., twisted fibers or cords). To better understand why, in such situations, high mechanical performances are obtained, an analytical model is herein proposed. It is based on a cohesive interface analysis, which has been largely adopted to investigate the mechanical response of FRC or the snubbing effects produced by inclined fibers, but not the condition of multiple cracking and strain hardening of HPFRCC. Through this approach, all the phenomena that affect the post-cracking response of FRC are evidenced, such as the nonlinear fracture mechanics of the matrix, the bond–slip behaviour between fibers and matrix, and the elastic response of both materials. The model, capable of predicting the average distance between cracks as measured in some experimental campaigns, leads to a new design criterion for HPFRCC and can eventually be used to enhance the performances of cement-based composites.

1. Introduction

Both in tension and in compression, the stress–strain curves of cementitious composites are similar in shape. After the first ascending branch, strain softening characterizes the failure stage of these materials, during which one or more cracks and localized strains can be detected. However, in the case of uniaxial tensile tests, the state of stress within the specimen makes the arrest of cracking impossible, and therefore the post-peak response exhibits low fracture toughness and the appearance of a single crack [1].

To avoid this brittle behaviour, steel reinforcing bars are generally placed in the tensile zones of concrete structures. The new composite structure can be exemplified by the reinforced concrete (RC) tie depicted in Fig. 1a [2], whose mechanical responses, in terms of applied load N *vs.* average steel strain ε_m , are illustrated in Fig. 1b–c. Depending on steel percentage ρ, defined as the ratio between the cross-sectional areas of rebars A_s and of surrounding concrete A_c (Fig. 1a), RC ties show different N–ε_m curves.

In the case of under-reinforced concrete structures (i.e., ρ lower than the minimum percentage ρ_{min}), when the cracking load N_{cr} is reached, a single crack rapidly develops [2]. As shown in Fig. 1b, the mechanical response is typically brittle, and the load at yielding of rebars N_y is lower than N_{cr} .

In the presence of higher reinforcement percentages ($\rho>\rho_{min}$), moderate softening appears after the formation of the first crack and, as the average steel strain ε_m increases, the applied normal force N tends to exceed the cracking load N_{cr}. At $N=N_{cr}$, assuming a uniform tensile strength f_{ct}, other cracks can develop before the yielding of rebars. In this case (Fig. 1c), the RC tie fails in a ductile manner ($N_y>N_{cr}$) and shows several cracks [2]. In other words, the presence of an adequate amount of reinforcement, makes multiple cracking possible and contributes to the increase of concrete fracture toughness (Fig. 1c). Contrary to the case of $\rho<\rho_{min}$ (Fig. 1b), a strain hardening behaviour characterizes the post-cracking stage of multi-fractured RC ties (Fig. 1c).

A ductile response under tensile loads can be achieved in cement-based composites reinforced with discontinuous fibers [3]. In the case of traditional concrete without any fibers (Fig. 2a), the stress–strain relationship σ_c–ε_c rapidly reaches the peak and shows subsequent softening branch, because of strain localization within a single crack. According to the fictitious crack model proposed by Hillerborg et al. [4], the post-cracking stage of uniaxial tensile test can be reproduced by stress–crack opening σ_c–w relationship (Fig. 2a).

* Corresponding author. Tel.: +39 011 5644889; fax: +39 011 5644899.
E-mail addresses: alessandro.fantilli@polito.it (A.P. Fantilli), mihashi@timos.str.archi.tohoku.ac.jp (H. Mihashi), paolo.vallini@polito.it (P. Vallini).
[1] Tel.: +81 22 795 7864; fax: +81 22 795 4772.
[2] Tel.: +39 011 5644889; fax: +39 011 5644899.

0008-8846/$ – see front matter © 2009 Elsevier Ltd. All rights reserved.
doi:10.1016/j.cemconres.2009.08.020

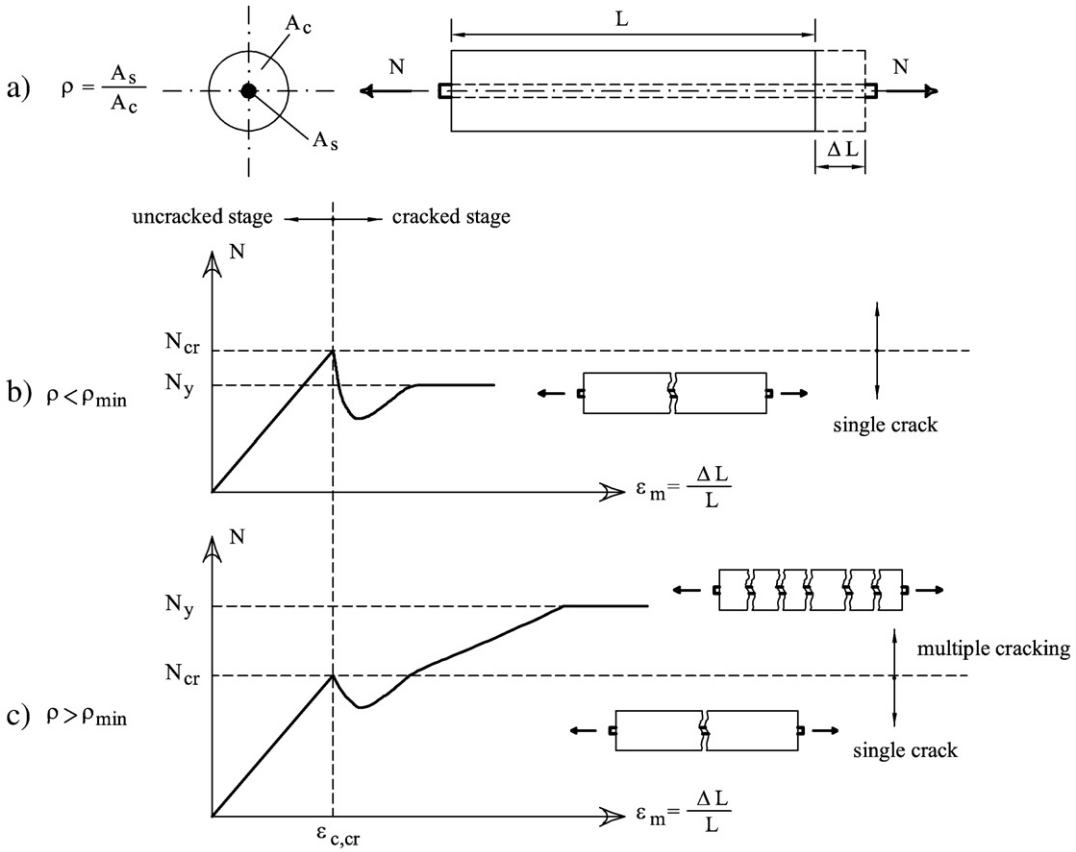

Fig. 1. Mechanical response of RC ties [2]: a) geometrical properties; b) N–ε_m diagram of under-reinforced ties ($\rho<\rho_{min}$); c) N–ε_m diagram of ordinary reinforced ties ($\rho>\rho_{min}$).

If fibers are added to the classical components of concrete, the new composite material can show higher fracture toughness under uniaxial tension. With respect to the RC tie of Fig. 1, in which rebars bridge tensile cracks with concentrate actions on cracked cross-sections, the fibers randomly dispersed in a cementitious matrix generate more distributed bridging stresses on crack surfaces. The magnitude of these stresses and, in general, the mechanical response of fiber-reinforced cementitious composites (FRC) strongly depend on the type and volume fraction V_f of fiber.

If a low amount of fibers ($V_f<1\%$) is added to the cement-based matrix, the post-peak behaviour of FRC does not much differ from that of plain concrete (Fig. 2b). As the tensile strength f_{ct} and the corresponding strain $\varepsilon_{c,cr}$ are reached, strain localizes in a single crack and the failure stage begins. Obviously, FRC show higher fracture toughness than traditional concrete (i.e., a wider area is delimited by the σ_c–w diagram of Fig. 2b), which gives relevant structural advantages during the serviceability and failure stages of massive tunnel linings [5,6].

In the case of high fiber volume fraction ($V_f>2\%$), FRC specimens subjected to uniaxial tensile loads show a strain hardening behaviour after the formation of the first crack. As a result, the tensile strength of the composite, f_{max}, is higher than that at first cracking f_{ct}. In addition, such FRC can be distinguished by the presence of several cracks in the post-cracking stage, when $\varepsilon_c>\varepsilon_{c,cr}$ and $f_{ct}<\sigma_c<f_{max}$ (Fig. 2c). Multiple cracking has been largely observed since the introduction of the asbestos–cement composites [7], which has been progressively replaced, for the last two decades, by environmental-friendly high ductile FRC. This is the case of the so-called High Performance Fiber-Reinforced Cementitious Composites (HPFRCC) [8], whose fiber volume fraction is generally lower than 2%. Under uniaxial tensile loads, HPFRCC specimens show very ductile behaviour and high fracture toughness, which are even comparable with those of aluminium alloys [9].

Multiple cracking and strain hardening regimes characterize the mechanical response of FRC (with $V_f>2\%$) and of HPFRCC specimens (Fig. 2c), as well as the post-cracking stage of ordinary RC ties (Fig. 1c). In all cases, after the formation of the first crack, an increase of the axial loads ($N>N_{cr}$ in the ties of Fig. 1c) and of the tensile stresses ($\sigma_c>f_{ct}$ in the composite of Fig. 2c) can be attained, if the pullout strength of rebars and fibers is higher than N_{cr} and f_{ct}, respectively. By increasing N, and σ_c, steel reinforcing bars, and fibers, transfer additional stresses to the surrounding concrete, and to cementitious matrix, as a consequence of bond stresses generated by slips between materials. If bond stresses are lower than the bond strength, other cracks take place in concrete and cementitious matrix. The process of crack formation ceases, if either failure or complete slippage of the reinforcement occurs [3].

Bond stress diffusion is the main aspect that needs to be modelled, both in RC ties (Fig. 1) and FRC specimens in tension (Fig. 2), if the multiple cracking and strain hardening phenomena have to be investigated. Depending on the way the bond–slip mechanism is taken into consideration, the models reported in the current literature can be classified into different groups [10]. Classical approaches assume that perfect bond persists till energy criterion is exceeded on the interface between rebars and concrete or between fiber and matrix. Thus, only when the energy release rate of a discontinue fiber composite is lower than a critical value, can the condition of strain hardening be satisfied [11]. This leads to the definition of the critical fiber volume fraction $V_{f,cr}$, which is proportional to the properties of a fiber-reinforced composite [12]:

$$V_{f,cr} \propto \frac{G_{tip}}{g\,\tau_{max} w_p \left(\frac{L_f}{d_f}\right)^2} \tag{1}$$

where, G_{tip} = crack tip critical energy release rate of the composite; τ_{max} = bond strength; g = snubbing coefficient which takes into

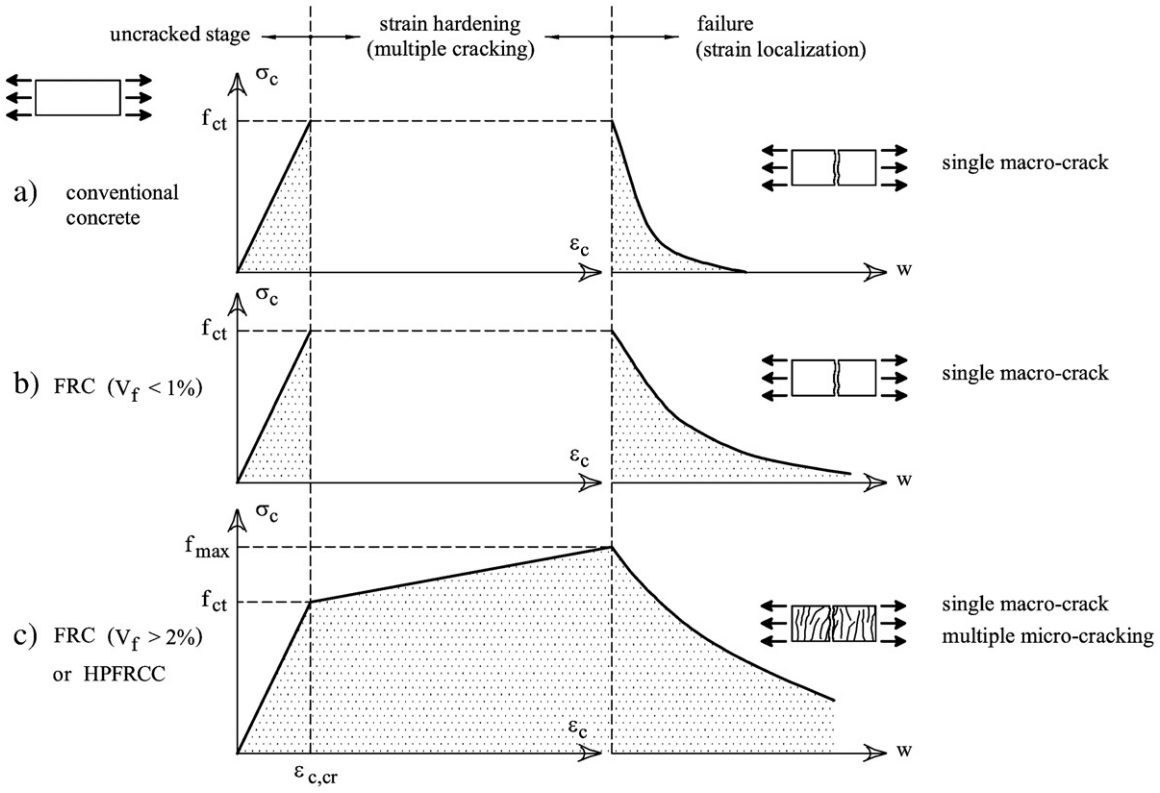

Fig. 2. Mechanical response of cement-based composites under uniaxial tension: a) σ_c–ε_c and σ_c–w diagrams of ordinary concretes; b) σ_c–ε and σ_c–w diagrams of FRC with low fiber volume fractions (V_f<1%); c) σ_c–ε and σ_c–w diagrams of HPFRCC and of FRC with high fiber volume fractions (V_f>2%).

account the effects due to misaligned fibers with respect to crack surface [13]; w_p = crack opening displacement corresponding to the maximum bridging stress; L_f = length of fiber; and d_f = diameter of fiber. Thus, strain hardening behaviour of FRC takes place when:

$$V_f \geq V_{f,cr}. \tag{2}$$

Moreover, if the following condition is satisfied [14]:

$$f_{ct} < f_{max} \tag{3}$$

additional cracks will form after the first cracking (Fig. 2c). The tensile strength f_{max} of the composite can be assumed as proportional to [14,15]:

$$f_{max} \propto \frac{V_f L_f g \tau_{max} p_f}{A_f} \tag{4}$$

where, p_f = perimeter of fiber cross-section; and A_f = cross-sectional area of fiber.

Eqs. (2)–(3) express the necessary and sufficient conditions that a fiber-reinforced cementitious composite has to satisfy if the ductile response of Fig. 2c is attained [14]. This behaviour is mainly related to fiber geometry, tensile strength [expressed in terms of f_{max} in Eq. (3), and G_{tip} in Eq. (1)], bond strength, and to fiber volume fraction.

However, if the similarity with RC ties (Fig. 1c) is taken into consideration, the bond–slip mechanism between materials plays a fundamental role also during the post-cracking response of fiber-reinforced cement-based composites (Fig. 2c). In accordance with the classical approaches to the analysis of bond between reinforcement and concrete (fib-Task Group Bond Models [16]), the cracking regime of FRC should also be influenced by the elastic properties of its components, and therefore by the Young's moduli of fiber E_s and matrix E_c. Although they have been taken into consideration in models capable of defining the stress–crack width relationship of FRC [17,18], these mechanical properties do not compare in Eqs. (1)–(4). For the above reasons, new material design criterion for predicting multiple cracking and strain hardening in FRC is here presented. It is based on a cohesive interface modelling of bond diffusion, in which bond stresses are only produced by slips between fibers and the surrounding cement-based matrix [10]. Such an approach, generally applied to RC structures, consists of the equilibrium and compatibility equations of the so-called tension-stiffening problem [19]. For instance, it has been used to define the minimum reinforcement of RC beams [20] and to investigate the pullout behaviour of inclined fibers [13]. In both cases, the mathematical solution of the problem is obtained by numerical iterative procedures. Conversely, a closed form solution is here introduced in order to obtain analytical equations for the analysis of strain hardening and multiple cracking regimes, in fiber-reinforced cementitious composites.

2. Modelling the post-cracking stage of FRC

The growth of more cracks in FRC members subjected to uniaxial tension (Fig. 2c) can be investigated by drawing an analogy with the behaviour of RC ties. Fiber is considered as the reinforcing bar ($A_s = A_f$) of an element in tension (Fig. 3a) having a single crack in the concrete area $A_c = A_f/V_f$ (in this way $V_f = \rho = A_f/A_c$). By increasing the crack width w, the mechanical response of this structure, in terms of N–w (Fig. 3c), is more or less similar to that depicted in Fig. 1b–c. It depends on slips between fiber and matrix, whose distribution $s(z)$ is qualitatively drawn in Fig. 3b.

In the case of fibers symmetrically situated with respect to the crack, the maximum slip is located in the cracked cross-section (where $s = w/2$), from which it progressively vanishes with the increase of the distance z

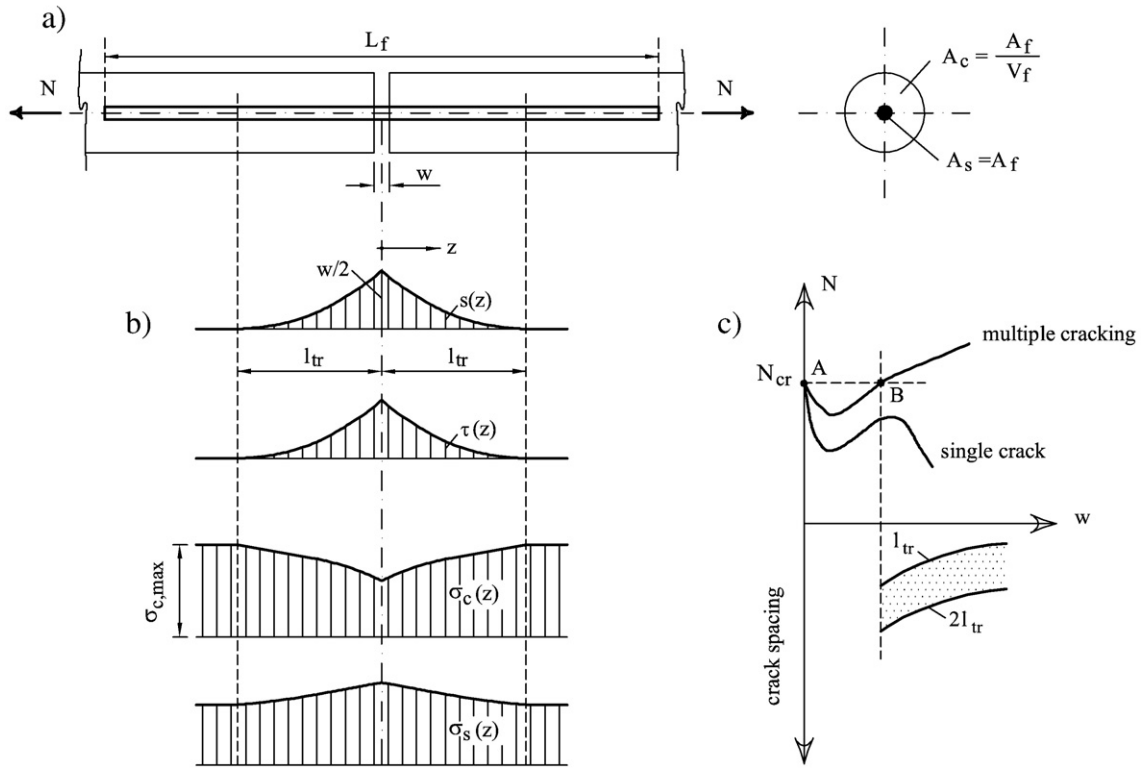

Fig. 3. The cohesive interface model for fiber–matrix interaction: a) geometrical properties of the structural element with a single crack; b) slip $s(z)$, bond stress $\tau(z)$, concrete stress $\sigma_c(z)$, and fiber stress $\sigma_s(z)$ distributions around the crack; c) mechanical response in terms of normal force *vs.* crack spacing *vs.* crack width.

from the crack. In particular, $s(z)=0$ if $z \geq l_{tr}$ (where l_{tr} = transmission length). As z increases, the tensile stresses of fiber, $\sigma_s(z)$, continuously transfer to the cementitious matrix, because of bond stresses $\tau(z)$ acting on the interface between materials. As a consequence, within the domain $0 \leq z \leq l_{tr}$, tensile stresses in the matrix, $\sigma_c(z)$, are higher far from the crack surfaces (Fig. 3b). Beyond the transmission length, neither slips nor bond stresses exist, and, therefore, the condition of perfect bond is verified when $z > l_{tr}$ (i.e., $\sigma_c = const$ and $\sigma_s = const$). In this zone, the stress in the cementitious matrix reaches the maximum value $\sigma_{c,max}$.

At onset of cracking, when $w \to 0$, $\sigma_{c,max}$ is generally lower than f_{ct} and the N–w diagram shows a softening branch (i.e., $N < N_{cr}$ in Fig. 3c). If these conditions persist for higher crack width, the failure of the structural element depicted in Fig. 3a occurs in the presence of a single tensile crack. Conversely, when $\sigma_{c,max} = f_{ct}$, which corresponds to the point B of Fig. 3c, new cracks appear and, with the increase of w, strain hardening characterizes the N–w diagram (i.e., $N \geq N_{cr}$). According to Fantilli et al. [19], during this stage, the average crack spacing ranges between l_{tr} and 2 l_{tr} (Fig. 3c). Under the condition of symmetry depicted in Fig. 3a–b, the multiple cracking regime is possible if the semi-length of the fiber is higher than the average crack spacing (i.e., $1.5\, l_{tr} < L_f/2$). In other words, the definition of l_{tr} at cracking load (i.e., at point B of the N–w diagram depicted in Fig. 3c) is of primary importance in the analysis of FRC elements in tension.

2.1. Equilibrium and compatibility equations for the tension-stiffening problem

In what follows, the analytical evaluation of the transmission length is obtained by adapting the tension-stiffening equations of RC structures to the fiber–matrix tie illustrated in Fig. 3a. As the present analysis is devoted to the definition of l_{tr}, and not of the crack profile, the hypothesis of plane cross-sections can be accepted [21]. Referring to the tie's portion depicted in Fig. 4a, the presence of linear and vertical strain profiles, defined by two different planes belonging to fiber and matrix, respectively, is assumed. At a distance z from the crack, slip is defined as the difference between the displacements of two planes (Fig. 4a):

$$s(z) = -[s_s(z) - s_c(z)] \tag{5}$$

where, s_s = displacement of fiber cross-section; and s_c = displacement of matrix cross-section.

If materials behave elastically, differentiating Eq. (5) with respect to z, one can obtain:

$$\frac{ds}{dz} = -(\varepsilon_s - \varepsilon_c) = -\frac{\sigma_s}{E_s} + \frac{\sigma_c}{E_c} \tag{6}$$

where, ε_s = tensile strains of fiber; and ε_c = tensile strain of matrix.

In a portion of length dz, the equilibrium equation of the reinforcing bar can be written as follows (Fig. 4b):

$$\frac{d\sigma_s}{dz} = -\frac{p_f \tau}{A_f} \tag{7}$$

where, τ = bond stress on the interface between fiber and concrete, which is a function of the slips s between materials.

In each cross-section of the considered tie (Fig. 4a), the global equilibrium condition must be satisfied:

$$N = \sigma_s A_f + \sigma_c A_c. \tag{8}$$

Eqs. (6)–(8) represent the mathematical formulation of the tension-stiffening problem applied to the structural element depicted in Fig. 3a. Since the first studies on bond and crack formation in RC elements [22], such a problem has been solved by reducing it to a

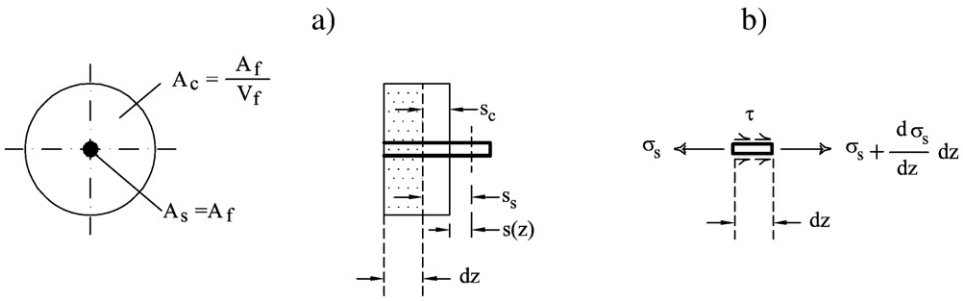

Fig. 4. An infinitesimal portion of fiber and matrix: a) displacements of matrix and fiber under the hypothesis of plane cross-sections; b) free-body diagram of the fiber.

single differential equation. In fact, if Eq. (6) and Eq. (8) are derived with respect to z, it is possible to obtain ($N = const$):

$$\frac{d^2 s}{dz^2} = -\frac{1}{E_s}\frac{d\sigma_s}{dz} + \frac{1}{E_c}\frac{d\sigma_c}{dz} \tag{9}$$

$$\frac{d\sigma_c}{dz} = -\frac{d\sigma_s}{dz}\frac{A_f}{A_c} = -\frac{d\sigma_s}{dz}V_f \tag{10}$$

where, $V_f = A_f/A_c$ = fiber volume fraction = ρ = geometrical percentage of reinforcement under the condition of $A_c = A_f/V_f$ (Fig. 3a).

The substitution of Eq. (10) into Eq. (9) yields:

$$\frac{d^2 s}{dz^2} = -\frac{d\sigma_s}{dz}\left(\frac{1}{E_s} + \frac{V_f}{E_c}\right). \tag{11}$$

If Eq. (7) is substituted into Eq. (11), the whole tension-stiffening phenomenon is represented by:

$$\frac{d^2 s}{dz^2} = \frac{p_f \tau}{A_f}\left(\frac{1}{E_s} + \frac{V_f}{E_c}\right). \tag{12}$$

Regardless of the function $\tau(z)$ and, thus, independently of the bond–slip relationship between fiber and matrix [22], the solution of the above second order differential equation represents the function $s(z)$ within the domain $0 \le z \le l_{tr}$ (Fig. 3a–b).

2.2. Stress–crack opening displacement relationship for cementitious matrix

Two boundary conditions must be introduced to solve Eq. (12). One of them should regard the cracked cross-section (i.e., the left border of the domain $0 \le z \le l_{tr}$), where a relationship between the slip s and the tensile stress σ_c has to be defined. By considering the fiber symmetrically situated with respect to the already formed crack, and according to the bilinear σ_c–w relationship proposed by the CEB-FIP Model Code [23] for cementitious concrete and mortar (Fig. 5a), stresses at the crack surfaces can be evaluated as follows:

$$\sigma_c = f_{ct}\left(1 - 0.85\frac{w}{w_c}\right) \quad \text{if } 0 \le w \le w_1 \tag{13a}$$

$$\sigma_c = 0.15 f_{ct}\left(1 - \frac{w - w_1}{w_c - w_1}\right) \quad \text{if } w_1 < w \le w_c \tag{13b}$$

$$\sigma_c = 0 \quad \text{if } w > w_c \tag{13c}$$

where, w = crack width = $2s$; and w_1, w_c = parameters defined as a function of compressive strength f_c and of maximum aggregate size d_a [23].

Since the present analysis regards the situation in which the first crack is growing (i.e., $w \to 0$) and other cracks are going to develop (point B in Fig. 3c), the fictitious crack model can be approximated by the first linear branch of Fig. 5a:

$$\sigma_c = f_{ct} - k_C w. \tag{14}$$

The cohesive parameters k_C of Eq. (14), in accordance with the σ_c–w relationship proposed by CEB-FIP Model Code [23], becomes:

$$k_C = \frac{0.85 f_{ct}}{w_1}. \tag{15}$$

2.3. Bond–slip between fiber and matrix

In addition to the fictitious crack model, also a bond–slip relationship between fiber and matrix must be defined. This is a necessity for every cohesive interface model [10], like that expressed by Eq. (12) in the domain $0 \le z \le l_{tr}$ (Fig. 3a).

For smooth steel fibers in a cementitious matrix, the τ–s relationship proposed by Fantilli and Vallini [13] can be adopted (Fig. 5b). It consists of an improvement and an extension of the classical model proposed by CEB-FIP Model Code [23] for smooth steel reinforcing bars. In particular, both for bars and fibers, a softening regime is introduced in conjunction with the size effect caused by fiber diameter. The ascending branch and the post-peak stage of the proposed bond–slip relationship are defined, respectively, by the following equations (Fig. 5b):

$$\tau = \tau_{max}\left(\frac{s}{s_1}\right)^{0.5} \quad \text{if } s \le s_1 \tag{16a}$$

$$\tau = \tau_{fin} + (\tau_{max} - \tau_{fin}) e^{k(s_1 - s)} \quad \text{if } s > s_1 \tag{16b}$$

where, s_1 = slip at bond strength; τ_{fin} = asymptotic value of bond stress; and k = coefficient. These parameters can be defined as functions of bond conditions, fiber manufacture (hot rolled or cold drawn), compressive strength of concrete f_c, and fiber diameter [13].

From a practical point of view, Eqs. (16a)–(16b) cannot be used for some kinds of fibers (e.g., twisted fibers) which show slip hardening. In addition, the micromechanics of crack bridging in FRC [17,18] also requires that the snubbing effects of misaligned fibers, as well as the cumulative effect of multiple fibers, are taken into account. According to Naaman [15], all the efficiency effects, as well as the bond between fiber and matrix, are in direct proportionality with the post-cracking stress of the FRC. In the present paper, only multiple cracking and strain hardening conditions have to be defined, thus bond stresses are those of the first ascending branch of τ–s (where slips are nearly zero). In other words, as the current analysis regards the element depicted in Fig. 3a, when $s \to 0$ and other cracks are going to develop (i.e., around the point B of Fig. 3c), bond stresses

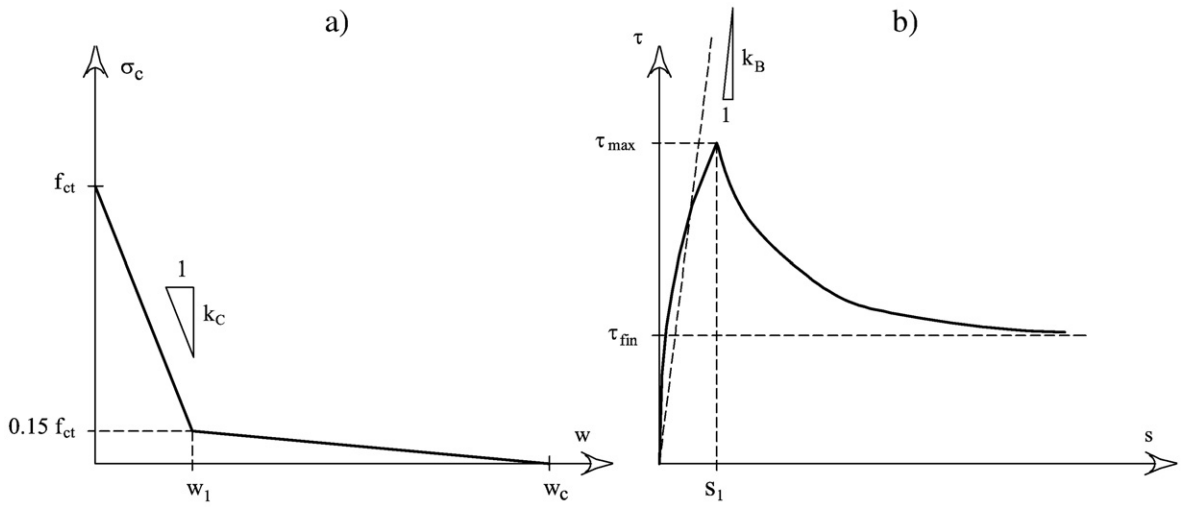

Fig. 5. The cohesive and bond parameters: a) fictitious crack model σ_c–w proposed by the CEB-FIP Model Code [23]; b) bond–slip τ–s relationship of smooth steel fibers in cementitious matrix [13].

are assumed to be in direct proportion with slips. Thus, to simplify the approach, the following linear model is here considered as the approximation of τ–s (Fig. 5b):

$$\tau = s k_B \tag{17}$$

where, k_B = bond parameter that needs to be evaluated experimentally.

There are two main advantages of using the simplified bond–slip relationship of Eq. (17). First of all, it is possible to consider k_B as the product of different factors, which include bond characteristics, snubbing, statistical distribution, and group effects of fibers. All these phenomena, which affect the mechanical response of FRC under tension, do not have to be measured separately through specific tests. Conversely, they are taken into account by a single bond parameter measured with uniaxial tensile tests on FRC.

2.4. An analytical equation for transmission length

If Eq. (17) is substituted into Eq. (12), the tension-stiffening problem of the fiber–matrix tie depicted in Fig. 3a is summarized by a linear differential equation:

$$\frac{d^2 s}{dz^2} - \alpha s = 0 \tag{18}$$

whose constant coefficient α depends on the following properties:

$$\alpha = \frac{p_f k_B}{A_f}\left(\frac{1}{E_s} + \frac{V_f}{E_c}\right) \tag{19}$$

The general solution of Eq. (18) is given by:

$$s(z) = C_1 e^{z\sqrt{\alpha}} + C_2 e^{-z\sqrt{\alpha}} \tag{20}$$

where the constants C_1 and C_2 are obtained by imposing the boundary conditions at the two borders of the domain $0 \le z \le l_{tr}$. More precisely, in the cracked cross-section (where $z = 0$), slip must be equal to the half of crack width, whereas at $z = l_{tr}$ slip should be equal to zero:

$$\begin{cases} s = w/2 & \text{if } z = 0 \\ s = 0 & \text{if } z = l_{tr} \end{cases}. \tag{21}$$

Under the above conditions, Eq. (20) becomes:

$$s(z) = \frac{w}{2\left(1 - e^{-2l_{tr}\sqrt{\alpha}}\right)}\left[-e^{(z-2l_{tr})\sqrt{\alpha}} + e^{-z\sqrt{\alpha}}\right]. \tag{22}$$

When the function $s(z)$ is known, stress distributions in both fiber and matrix can be calculated. In particular, by substituting Eq. (7) and Eq. (17) into Eq. (10), the derivative of tensile stresses σ_c is also defined:

$$\frac{d\sigma_c}{dz} = \frac{p_f k_B V_f}{A_f} s(z). \tag{23}$$

If Eq. (22) is substituted into Eq. (23), a first order differential equation can be written:

$$\frac{d\sigma_c}{dz} = + \frac{p_f k_B V_f}{A_f} \frac{w}{2\left(1 - e^{-2l_{tr}\sqrt{\alpha}}\right)}\left[-e^{(z-2l_{tr})\sqrt{\alpha}} + e^{-z\sqrt{\alpha}}\right]. \tag{24}$$

The integration of Eq. (24) yields:

$$\sigma_c(z) = C_3 - \frac{p_f k_B V_f}{A_f} \frac{w}{2\left(1 - e^{-2l_{tr}\sqrt{\alpha}}\right)\sqrt{\alpha}}\left[e^{(z-2l_{tr})\sqrt{\alpha}} + e^{-z\sqrt{\alpha}}\right] \tag{25}$$

where the constant C_3 is obtained by imposing Eq. (14) on crack surfaces (where $z = 0$). Thus, the coefficient C_3 is computed as:

$$C_3 = f_{ct} - k_C w + \frac{p_f k_B V_f}{A_f} \frac{w}{2\left(1 - e^{-2l_{tr}\sqrt{\alpha}}\right)\sqrt{\alpha}}\left[e^{-2l_{tr}\sqrt{\alpha}} + 1\right] \tag{26}$$

and, consequently, Eq. (25) provides the distribution of tensile stresses in the cementitious matrix within the transmission length:

$$\sigma_c(z) = f_{ct} - k_C w + \frac{p_f k_B V_f}{A_f} \frac{w}{2\left(1 - e^{-2l_{tr}\sqrt{\alpha}}\right)\sqrt{\alpha}}\left[e^{-2l_{tr}\sqrt{\alpha}} + 1 - e^{(z-2l_{tr})\sqrt{\alpha}} - e^{-z\sqrt{\alpha}}\right]. \tag{27}$$

At $N = N_{cr}$ (point B in Fig. 3c), the condition of multiple cracking is achieved in the element depicted in Fig. 3a, and the

maximum tensile stress of the matrix equates the tensile strength f_{ct}, i.e.,

$$\sigma_c = f_{ct} \text{ if } z = l_{tr}. \tag{28}$$

In the above situation, Eq. (27) becomes:

$$0 = -k_C + \frac{p_f k_B V_f}{A_f} \frac{\left(e^{-2ltr\sqrt{\alpha}} + 1 - 2e^{-ltr\sqrt{\alpha}}\right)}{2\left(1 - e^{-2ltr\sqrt{\alpha}}\right)\sqrt{\alpha}}. \tag{29}$$

Eq. (29) gives the transmission length l_{tr}, which is the solution of the problem, independently of crack width w. By introducing the following coefficient:

$$\beta = \frac{p_f k_B V_f}{2A_f k_C \sqrt{\alpha}} \tag{30a}$$

and a new dummy variable:

$$x = e^{-ltr\sqrt{\alpha}} \tag{30b}$$

Eq. (29) simply becomes an algebraic quadratic equation:

$$(\beta + 1)x^2 - 2\beta x + (\beta - 1) = 0. \tag{31}$$

The two solutions of Eq. (31) are given by:

$$\begin{cases} x_1 = \dfrac{\beta - 1}{\beta + 1} \\ x_2 = 1 \end{cases} \tag{32}$$

which respectively provide the following values of the transmission length:

$$l_{tr} = -\frac{\ln \frac{\beta - 1}{\beta + 1}}{\sqrt{\alpha}} \tag{33a}$$

$$l_{tr} = 0. \tag{33b}$$

Referring to the N–w diagram of Fig. 3c, at $N = N_{cr}$ there are two possible transmission lengths. One of them ($l_{tr} = 0$) determines the situation of an undeveloped crack ($w = 0$) and corresponds to the point A of Fig. 3c. Conversely, the transmission length given by Eq. (33a) (i.e., $l_{tr} > 0$) corresponds to a single developed crack ($w > 0$) while other cracks are going to appear (point B in Fig. 3c). According to Fantilli and Vallini [2] and to Fantilli et al. [19], the multiple cracking regime, which starts from the point B of N–w, can be simply described by this value of transmission length. To be more precise, l_{tr} [obtained with Eq. (33a)] and $2l_{tr}$ are, respectively, the minimum and the maximum distance between cracks in a FRC element in tension.

The proposed adaptation of a tension-stiffening problem to FRC can be accepted if materials show linear elastic behaviours. This is always true for the uncracked cementitious matrix, whereas it should be checked each time for the fiber. For the sake of simplicity, at incipient cracking, it is sufficient to verify whether or not tensile stresses in the fiber cross-section, $\sigma_{s,cr}$, are lower than the fiber strength f_u. Under the hypothesis of uncracked matrix, this condition yields:

$$\sigma_{s,cr} = E_s \varepsilon_{c,cr} = E_s \frac{f_{ct}}{E_c} < f_u. \tag{34}$$

Finally, some comments about the symmetrical position of the fiber with respect to crack (Fig. 3a) have to be made. This hypothesis is admissible if the transmission length obtained with Eq. (33a) is considerably lower than fiber length. In fact, in such case, slips and stresses are symmetrically distributed around each cracked cross-section (Fig. 3a). However, the conditions of multiple cracking and strain hardening require short distances between cracks, and, consequently, short transmission lengths. Thus, the ideal distributions of $s(z)$, $\sigma_c(z)$ and $\sigma_s(z)$, depicted in Fig. 3b, are admissible in the present analysis, where the multiple cracking regime of FRC is investigated.

3. Analytical results and experimental data

Cementitious composites tailored to enhance both multiple cracking and strain hardening can be reinforced with different kinds of fibers. For instance, in the specimens tested by Rinaldi and Grimaldi [24] under uniaxial tension, large fiber volume fractions ($V_f = 5\%$) of steel fibers with hooked ends (Fig. 6a) have been added to a cement-based matrix. In other FRCs, high performances have been achieved in presence of lower fiber volume fractions. This is the case of the HPFRCC reinforced with 2% in volume of Torex fibers [15], which are twisted steel fibers with triangular cross-sections (Fig. 6b).

Another high performance fiber-reinforced concrete, named ECC (Engineered Cementitious Composite), has been introduced by Li [25]. It is made by 2% in volume of PVA (PolyVinyl Alcohol) fibers dispersed in a cementitious matrix. In this case, the fiber aspect ratio (i.e., the ratio between L_f and d_f) is even higher than that of asbestos fibers (Fig. 6c), which were generally used to reinforce asbestos–cement composites [7].

In the following sections, the proposed model is applied in all the aforementioned fiber-reinforced cementitious composites in order to predict the distances between cracks measured during multiple cracking regime.

3.1. FRCs made with steel fibers with hooked ends

Steel fibers with hooked ends are the most commonly used to reinforce cementitious composites. When added in high volume fractions ($V_f > 2\%$), they can guarantee multiple cracking and strain hardening under uniaxial tension (Fig. 2c). However, such phenomena are not only a function of V_f, but also of other material properties. This is evidenced by the specimens (named H1, H2 and H3) depicted in Fig. 7a [26,27], and by Rinaldi's and Grimaldi's [24] bone shaped elements (named H4 and H5) reported in Fig. 7b. Table 1 summarizes the geometrical and mechanical properties of the five specimens.

In the specimens H1, H2, and H3, which show strain hardening response after the formation of the first crack, the average distances between the cracks have been measured during the multiple cracking regime. Their values can be compared with the analytical results of the proposed model. As illustrated in Fig. 8a, for the specimens H1 and H2, made of high strength matrix ($f_c = 84$ MPa), and in Fig. 8b for the specimen H3, made of normal strength matrix ($f_c = 49$ MPa), the possible evolution of crack spacing is here related to fiber volume fraction. In this way, the range defined by the curves l_{tr}–V_f and $2l_{tr}$–V_f should encompass the experimental values of crack spacing, as stated by Fantilli and Vallini [2] and by Fantilli et al. [19].

Referring to the specimens H1 and H2, the transmission length at each V_f is calculated with Eq. (33a) and the data reported in Table 1. The cohesive parameter $k_C = 393$ MPa/mm is computed with Eq. (15), whereas $k_B = 3500$ MPa/mm is obtained by best-fitting numerical and experimental values of crack spacing. The range obtained with the proposed approach is depicted in Fig. 8a. It represents a good estimation of the real distance between cracks during the strain hardening regime.

It must be observed that the theoretical range does not exist when the fiber volume fraction is larger than a critical value ($V_{f,cr} = 0.94\%$ for the specimens H1 and H2). In other words, if $V_f < V_{f,cr}$, multiple cracking regime is no longer possible, because the transmission length analytically calculated with Eq. (33a) becomes infinitely long. Thus, in the specimen H1, whose V_f is slightly higher than $V_{f,cr}$, more than one

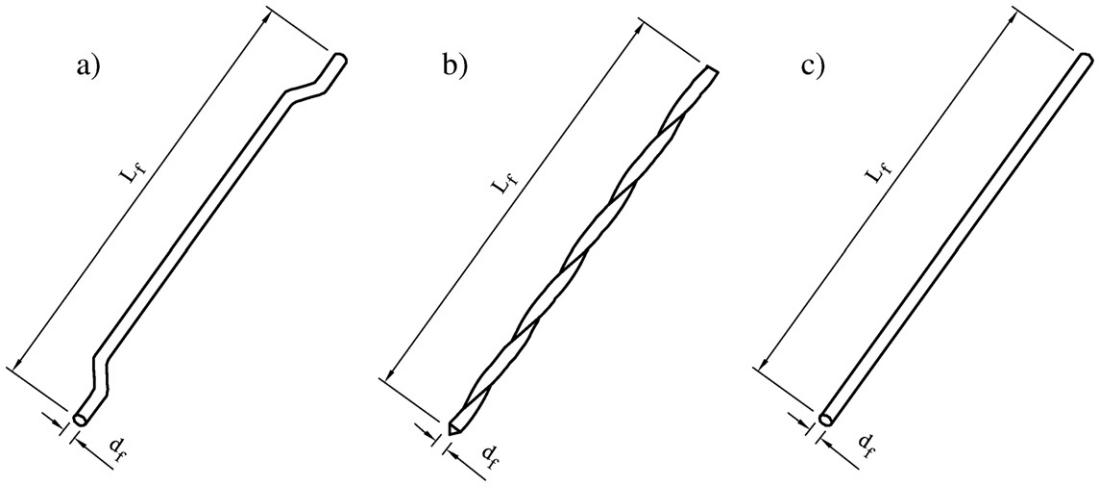

Fig. 6. Three types of fibers: a) smooth steel fibers with hooked ends; b) twisted steel fibers with triangular cross-sections —Torex [15]; c) PVA [25] or asbestos fibers [7].

crack appears in the post-cracking stage. This ductile response is also facilitated by the presence of a distance between cracks lower than $L_f/2$ (see Table 1 and Fig. 8a).

The possible range of crack spacing, delimited by the analytical functions l_{tr}–V_f and $2l_{tr}$–V_f, is also calculated for the specimen H3 (Fig. 8b). In this case, the bond parameter already estimated for the specimens H1 and H2 ($k_B = 3500$ MPa/mm) is assumed. In fact, for the same type of fiber, independently of the matrix strength, the τ–s relationship remains unchanged in the first stage, when $s \to 0$ [13]. On the contrary, a new cohesive parameter ($k_C = 780$ MPa/mm) is obtained from Eq. (15) and the data reported in Table 1. The average distance between cracks measured by Kim et al. [26] for the specimen H3 falls within the range obtained with the proposed approach. With respect to the case of Fig. 8a, the critical value of fiber volume fraction is approximately doubled ($V_{f,cr} = 1.96\%$), and, consequently, just a single crack appears if $V_f = 1\%$ (Fig. 8b).

The possible variation of crack spacing has been also evaluated for the specimens H4 and H5 depicted in Fig. 7b. In this case, the two curves reported in Fig. 9 (i.e., l_{tr}–V_f and $2l_{tr}$–V_f) have been computed by considering the bond parameter already adopted for steel fibers with hooked ends ($k_B = 3500$ MPa/mm). Eq. (15) and the data reported in Table 1 have been used to calculate a new cohesive parameter ($k_C = 326$ MPa/mm). Without measuring the distance between cracks, Rinaldi and Grimaldi [24] have observed both multiple cracking and strain hardening regimes in the specimen H5. Conversely, they have noticed a strain softening response in the post-cracking stage of the specimen H4, which collapses in the presence of a single crack. This is in accordance with the results of the proposed model (Fig. 9), even though the computed critical value of fiber volume fraction ($V_{f,crit} = 0.93\%$) is lower than the fiber volume content ($V_f = 1\%$). In fact, the average crack spacing estimated for the specimen H4 is higher than the half-length of the adopted fiber (Fig. 9).

In all the five FRC specimens, the failure of fibers at first cracking is definitely avoided. This is confirmed by the last column of Table 1, where the reported values of $\sigma_{s,cr}$ [Eq. (34)] are lower than f_u.

3.2. FRCs made with twisted steel fibers

Compared to other steel fibers on the market, Torex fibers (Fig. 6b) show higher performances and, in particular, larger pullout energies. This is due to the presence of higher bond stresses on the interface between materials, which can be detected even when the complete slippage of the fiber is going to occur [15]. As a result, cementitious composites reinforced with Torex tend to exhibit both strain hardening and multiple cracking regimes. This is confirmed by the uniaxial tensile tests conducted by Kim et al. [26,27] on the specimens depicted in Fig. 7a (and named T1, T2 and T3 in Table 2). They have the same fiber volume fraction and more or less the same cementitious matrix of the specimens

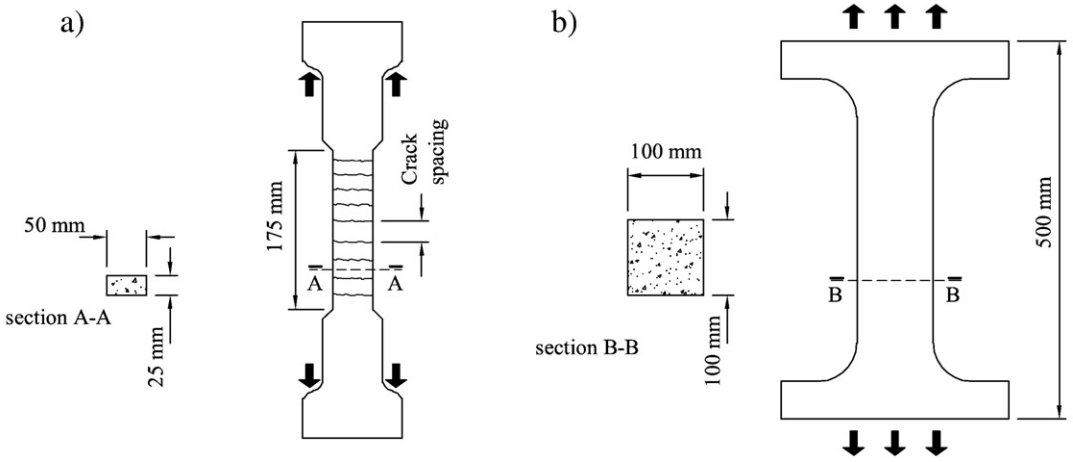

Fig. 7. Uniaxial tensile tests on cement-based composites: a) specimens reinforced with hooked steel fibers or Torex fibers [26,27]; b) specimens reinforced with hooked steel fibers [24].

Table 1
Mechanical and geometrical properties of the specimens reinforced with hooked steel fibers.

Specimen	Reference	Fiber					Matrix				Crack pattern		$\sigma_{s,cr}$ (MPa)
		d_f (mm)	L_f (mm)	f_u (MPa)	E_s (GPa)	V_f (%)	f_c (MPa)	f_{ct} (MPa)	E_c (GPa)	d_a (mm)	Multiple cracking	Crack spacing (mm)	
H1	Kim et al. [27]	0.38	30.0	2300	200	1.0	84.0	4.2	43.7(*)	2.0(°)	Yes	11.85	19.2
H2	Kim et al. [27]	0.38	30.0	2300	200	2.0	84.0	4.2	43.7(*)	2.0(°)	Yes	6.56	19.2
H3	Kim et al. [26]	0.40	30.0	2100	200	2.0	49.0	4.9(+)	36.5(*)	2.0(°)	Yes	11.85	26.8
H4	Rinaldi and Grimaldi [24]	0.56	30.0	–	200	1.0	25.0	2.5(+)	36.5(*)	2.0(°)	No	–	17.6
H5	Rinaldi and Grimaldi [24]	0.56	30.0	–	200	5.0	25.0	2.5(+)	36.5(*)	2.0(°)	Yes	–	17.6

(*)Estimated [23]; (°)estimated [1]; (+)estimated as 0.1 f_c.

H1, H2 and H3 (Table 1), respectively. However, as measured experimentally, a reduced distance between cracks (of about 30%) can be detected in all the specimens reinforced with Torex fiber (compare the values of crack spacing reported in Table 1 and Table 2).

Referring to the specimens T1 and T2 [27], Fig. 10a shows the curves l_{tr}–V_f and $2l_{tr}$–V_f, which delimit the proposed range of crack spacing. The evaluation of the transmission length, analytically calculated with Eq. (33a), requires the definition of both cohesive and bond parameters. Through Eq. (15) and the data reported in Table 2, the value $k_C = 580$ MPa/mm has been obtained for the specimens T1 and T2. At the same level of slip between fiber and matrix, Torex fibers generate higher bond stresses and consequently higher bond parameter k_B. This can be estimated from the best fit between experimental and analytical values of crack spacing. In particular, if $k_B = 4300$ MPa/mm, the range depicted in Fig. 10a represents a good approximation of the experimental data. Despite different values of k_C and k_B, the critical fiber volume fractions obtained for the specimens T1 and T2 ($V_{f,cr} = 0{,}97\%$) and for the specimens H1 and H2 ($V_{f,cr} = 0.94\%$) are more or less the same. However, the ranges of crack spacing are remarkably different, as illustrated by Fig. 8a and Fig. 10a. The narrower range reported in Fig. 10a, further confirms the tendency of Torex fibers, when used as reinforcement of cementitious matrix, to favour the trigger of more cracks and to reduce their spacing.

Fig. 10b shows the possible distances between cracks analytically calculated for the specimens T3 (Table 2) at different fiber volume fraction V_f. In this case, the curves l_{tr}–V_f and $2l_{tr}$–V_f have been obtained by assuming the same cohesive parameter ($k_C = 780$ MPa/mm) adopted for the specimen H3 (T3 and H3 have the same cementitious matrix), and the same bond parameter ($k_B = 4300$ MPa/mm) estimated for the specimens T1 and T2 (they are reinforced with the same type of fibers). The average crack spacing, experimentally measured for the specimen T3 by Kim et al. [26], falls within the range evaluated by the proposed model. In addition, with respect to the specimen H3 (Fig. 8b), Fig. 10b shows a narrower range and a lower value of critical fiber volume fraction ($V_{f,cr} = 1.33\%$). Thus, also in this case, the best performances of the specimens reinforced with Torex fibers are evidenced.

Finally, as confirmed by the last column of Table 2, in all the cement-based specimens reinforced with Torex, the condition $\sigma_{s,cr} < f_u$ is always satisfied.

3.3. FRCs made with PVA fibers and asbestos fibers

To favour the presence of multiple cracking in FRC elements subjected to uniaxial tension, straight PVA fibers (Fig. 6c) can be used as reinforcement. These cement-based composites, called with the acronym PVA-ECC (PolyVinyl Alcohol-Engineered Cementitious Composites), are reinforced with 2% in volume of PVA fibers, coated by 1% in volume of oiling agent [28,29].

Three PVA-ECC specimens (named E1, E2 and E3), reported in Table 3 and tested in accordance with the test arrangement depicted in Fig. 11a [28,29], are here used to validate the model. Their mechanical and geometrical properties are reported in Table 3, whereas the range of possible crack spacing is depicted in Fig. 11b. As in the previous cases, transmission lengths are analytically calculated with Eq. (33a), by assuming suitable values for k_C and k_B, and by varying the fiber volume fraction. Specifically, the cohesive parameter ($k_C = 510$ MPa/mm) has been computed from Eq. (15) and the data reported in Table 3, whereas the bond parameter ($k_B = 900$ MPa/mm) has been estimated by best-fitting analytical and experimental values of crack spacing (specimen E3 in Table 3). The curves l_{tr}–V_f and $2l_{tr}$–V_f, depicted in Fig. 11b, limit a very narrow range and define $V_{f,cr} = 1.7\%$. As remarked in the previous sections, if $V_f < V_{f,cr}$, there is not any possibility of multiple cracking. This is confirmed by the tests conducted by Yang et al. [29] on the specimens E1 ($V_f = 0.1\%$) and E2 ($V_f = 0.5\%$), whose brittle failure is produced by growing of a single crack.

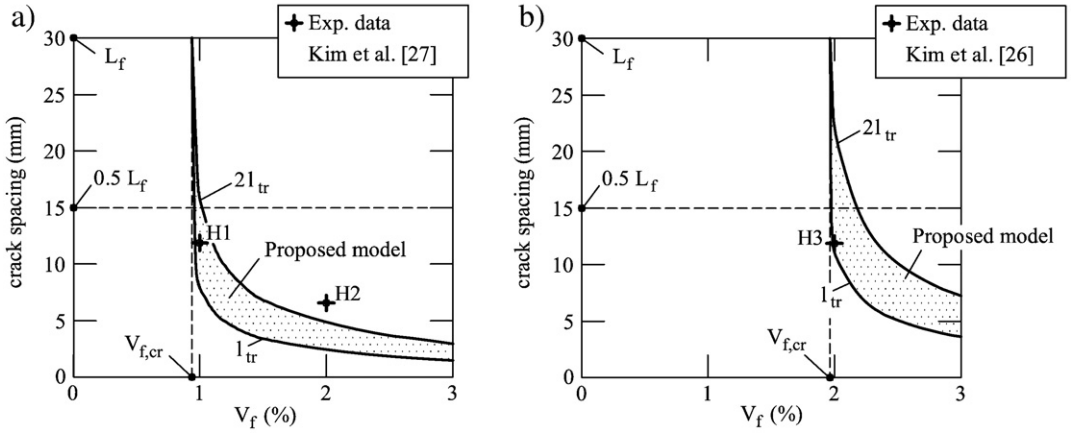

Fig. 8. Comparison between the results of the proposed model and the experimental data measured on specimens reinforced with hooked steel fibers [26,27]: a) crack spacing *vs.* fiber volume fraction V_f for the specimens H1 and H2 (Table 1); b) crack spacing *vs.* volume fraction V_f for the specimen H3 (Table 1).

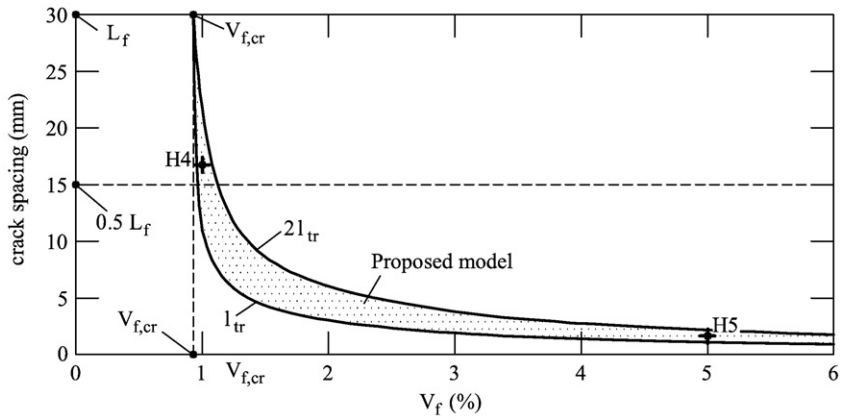

Fig. 9. The analytical range of crack spacing for the specimens H4 and H5 tested by Rinaldi and Grimaldi [24].

The range of crack spacing reported in Fig. 11b is analytically evaluated also in the case of high fiber volume fractions (V_f>10%) in order to compare the uniaxial tensile response of PVA-ECC with that of asbestos–cement composites. To this end, the specimen A1 tested by Akers and Garrett [7], and reinforced with asbestos fibers, is taken into consideration. The few known characteristics of this FRC are reported in Table 3, where they can be compared directly with the mechanical and geometrical properties of the specimens E1, E2 and E3 tested by Li et al. [28] and Yang et al. [29]. As PVA and asbestos fibers have the same diameter, the cohesive and bond parameters already estimated for PVA-ECC (i.e., k_C = 510 MPa/mm and k_B = 900 MPa/mm) are here considered valid also for asbestos–cement composites. Under these hypotheses, the analytical curves l_{tr}–V_f and $2l_{tr}$–V_f range the very narrow crack spacing of the specimen A1, which was experimentally measured by means of a scanning electronic microscope [7].

The average length of asbestos fibers (L_f = 3 mm) is generally shorter than the common fiber. Therefore, only in case of high fiber volume fraction (V_f>~6%) can the multiple cracking regime of asbestos cement composites originate. On the contrary, with the PVA fibers adopted by Li and co-workers, having the same diameter as asbestos fiber but with a greater length (L_f = 12 mm), the volume V_f = 2% is sufficient to obtain a very ductile behaviour under uniaxial tensile loads [28,29].

Finally, both the PVA-ECC and the asbestos–cement specimens reported in Table 3 satisfy Eq. (34) (see the last column of Table 3). Consequently, the fiber failures during the growth of the first tensile cracks are definitely avoided in both composites.

4. A new criteria for multiple cracking

For the fibers previously considered, the coefficient k_B of the simplified bond–slip model [Eq. (17)] is assumed to be constant for all the specimens reinforced with hooked end fibers (k_B = 3500 MPa/mm), with Torex fibers (k_B = 4300 MPa/mm), and with PVA and asbestos

Table 2
Mechanical and geometrical properties of the specimens reinforced with Torex fibers.

Specimen	Reference	Fiber					Matrix				Crack pattern		$\sigma_{s,cr}$ (MPa)
		d_f (mm)	L_f (mm)	f_u (MPa)	E_s (GPa)	V_f (%)	f_c (MPa)	f_{ct} (MPa)	E_c (GPa)	d_a (mm)	Multiple cracking	Crack spacing (mm)	
T1	Kim et al. [27]	0.3$^{(-)}$	30.0	2760	200	1.0	84.0	5.1	43.7$^{(*)}$	2.0$^{(°)}$	Yes	7.74	23.3
T2	Kim et al. [27]	0.3$^{(-)}$	30.0	2760	200	2.0	84.0	5.1	43.7$^{(*)}$	2.0$^{(°)}$	Yes	4.56	23.3
T3	Kim et al. [26]	0.3$^{(-)}$	30.0	2760	200	2.0	49.0	4.9$^{(+)}$	36.5$^{(*)}$	2.0$^{(°)}$	Yes	2.96	26.8

$^{(-)}$Equivalent diameter [15]; $^{(*)}$estimated [23]; $^{(°)}$estimated [1]; $^{(+)}$estimated as 0.1 f_c.

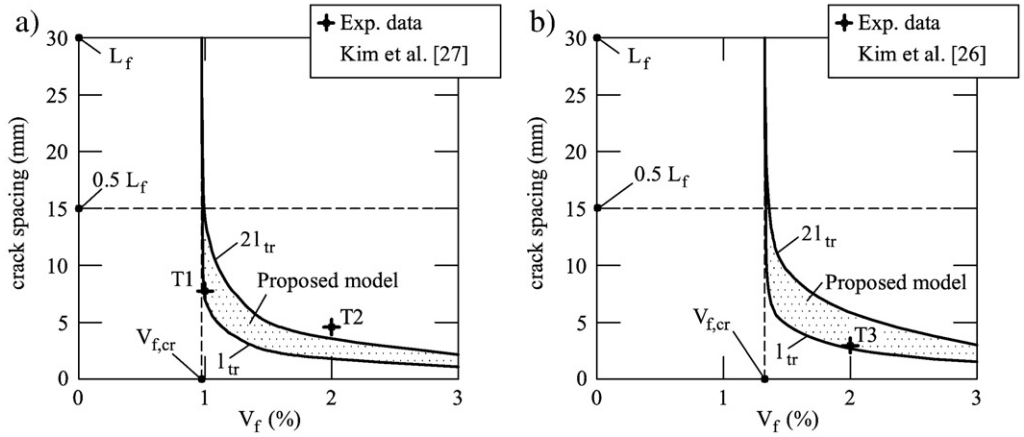

Fig. 10. Comparison between the results of the proposed model and the experimental data measured on specimens reinforced with Torex fibers [26,27]: a) crack spacing *vs.* fiber volume fraction V_f for the specimens T1 and T2 (Table 2); b) crack spacing *vs.* fiber volume fraction V_f for the specimen T3 (Table 2).

Table 3
Mechanical and geometrical properties of the specimens made of PVA-ECC and asbestos–cement composites.

Specimen	Reference	Fiber					Matrix				Crack pattern		$\sigma_{s,cr}$ (MPa)
		d_f (mm)	L_f (mm)	f_u (MPa)	E_s (GPa)	V_f (%)	f_c (MPa)	f_{ct} (MPa)	E_c (GPa)	d_a (mm)	Multiple cracking	Crack spacing (mm)	
E1	Yang et al.[29]	0.039	12.0	1600	40	0.1	29.0$^{(+)}$	2.9	30$^{(*)}$	0.15	No	–	3.78
E2	Yang et al. [29]	0.039	12.0	1600	40	0.5	29.0$^{(+)}$	2.9	30$^{(*)}$	0.15	No	–	3.78
E3	Li et al. [28]	0.039	12.0	1600	40	2	29.0$^{(+)}$	2.9	30$^{(*)}$	0.15	Yes	2.8	3.78
A1	Akers and Garrett [7]	0.04	3.0	–	–	10	–	–	–	–	Yes	0.45	3.78

$^{(*)}$Estimated [23]; $^{(+)}$estimated as 10 f_{ct}.

fibers (k_B = 900 MPa/mm). In all the cases, k_B has been easily measured by means of uniaxial tensile tests on FRC, without considering pullout tests. The good agreement between numerical results and experimental data not only validates the proposed model, but also confirms the possibility of taking into account some of the micromechanics phenomena (snubbing effects, cumulative effects of multiple fibers, etc.) within the single bond parameter k_B. Moreover, the results of the proposed approach, which agree with the data measured in different HPFRCCs, show the importance of fiber volume fraction, and in particular its critical value $V_{f,cr}$. According to Li and Leung [11], if $V_f < V_{f,cr}$ the strain hardening behaviour of FRC in the post-cracking stage is practically impossible. However, recalling Eq. (1), $V_{f,cr}$ is here computed by following the cohesive interface approach introduced for the evaluation of transmission length. More specifically, independently of fiber length, the critical fiber volume fraction must produce $l_{tr} \to \infty$ at the onset of cracking. If Eq. (33a) is used to compute the transmission length, the above condition is satisfied when:

$$\beta = \frac{p_f k_B V_{f,cr}}{2A_f k_C \sqrt{\alpha}} = \frac{p_f k_B V_{f,cr}}{2A_f k_C \sqrt{\frac{p_f k_B}{A_f}\left(\frac{1}{E_s} + \frac{V_{f,cr}}{E_c}\right)}} = 1. \tag{35}$$

Eq. (35) can be transformed into the following algebraic quadratic equation:

$$(V_{f,cr})^2 \frac{p_f k_B}{A_f 4 (k_C)^2} - \frac{(V_{f,cr})}{E_c} - \frac{1}{E_s} = 0 \tag{36}$$

whose positive solution gives the critical value of fiber volume fraction:

$$V_{f,cr} = \frac{A_f 2 (k_C)^2}{E_c p_f k_B}\left(1 + \sqrt{1 + \frac{(E_c)^2 p_f k_B}{A_f E_s (k_C)^2}}\right). \tag{37}$$

With respect to the energetic approach [Eq. (1)], this new formula furnishes a different critical fiber volume fraction. As a matter of fact, the elastic properties of materials (i.e. the Young's moduli E_s and E_c of fiber and matrix, respectively) are included in Eq. (37).

Based on the proposed approach, new conditions from multiple cracking and strain hardening regimes can also be introduced:

$$V_f > V_{f,cr} \tag{38a}$$

$$S_{r,m} = 1.5 l_{tr} < \frac{L_f}{2} \tag{38b}$$

where $s_{r,m}$ = average crack spacing at cracking load N_{cr}.

In a given FRC, Eqs. (38a)–(38b) are both satisfied when:

$$l_{tr} \to 0 \quad \text{and} \quad V_{f,cr} \to 0 \tag{39a}$$

or, according to Eq. (33a) and Eq. (35), when

$$\beta \gg 1 \tag{39b}$$

In other words, the post-cracking response of cement-based specimen subjected to uniaxial tension only depends on the properties that define the coefficient β [Eq. (30a)]. As the value of β must be far greater than 1 in very ductile fiber-reinforced concrete, the conditions stated by Eqs. (38a)–(38b) are both satisfied when:

$$\frac{V_f}{k_C}\sqrt{\frac{p_f}{A_f} k_B} \gg 2\sqrt{\frac{1}{E_s} + \frac{1}{E_c} V_f}. \tag{40}$$

Eq. (40) represents a new criterion to optimize the cost and the performances of fiber-reinforced composites. For instance, to increase the fracture toughness with the same fiber volume fraction ($V_f > V_{f,cr}$), fibers with a higher p_f/A_f ratio can be introduced. This is the case of Torex fibers [15] with triangular cross-sections (Fig. 6b). Similarly, it is possible to increase the fiber aspect ratio L_f/d_f, as done in the older asbestos cement composites [7] and in the more environmental-friendly PVA-ECC [25].

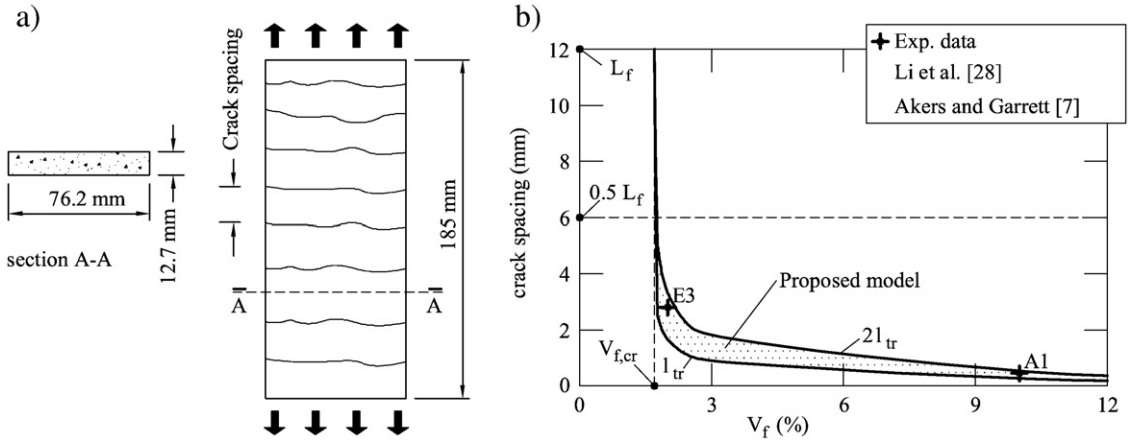

Fig. 11. Comparison between the results of the proposed model and the experimental data measured by Li et al., [28], Yang et al. [29], and Akers and Garrett [7]: a) PVA-ECC specimens under uniaxial tension; b) crack spacing *vs.* fiber volume fraction V_f for the five specimens reported in Table 3.

Regarding the bond properties, concrete fracture toughness can be augmented by using fibers with higher bond parameter k_B. This is evidenced by the cementitious composites reinforced with twisted fibers [15].

Moreover, Eq. (40) suggests low cohesive parameters k_C (i.e. the cementitious matrix should be the least brittle as possible). If Eq. (15) is used to calculate k_C, tensile strength f_{ct} and, consequently, compressive strength f_c need to be reduced. However, such reductions produce very brittle cementitious composites and shorter w_1 (see Fig. 5a) [23]. Finally, with respect to classical approaches, Eq. (40) also recommends the increment of the Young's moduli E_s and E_c.

5. Conclusions

New criteria for the definition of multiple cracking and strain hardening regimes in fiber-reinforced cementitious composites can be derived from the analysis of bond–slip between fibers and matrix. By means of the proposed cohesive interface approach, it is possible to predict the crack spacing observed in very ductile specimens in tension. Based on the results presented in the previous sections, the main aspects of modelling the post-cracking stage of FRC can be summarized by the following points:

- According to several tests, the average distance between cracks is ranged by once and twice the transmission length analytically evaluated with Eq. (33a).
- At cracking load, the value of the transmission length, and the consequent presence of multiple cracking regime, is independent of crack width.
- A new formula [Eq. (37)] for the critical value of fiber volume fraction is here introduced to define the lower bound amount of fiber. If $V_f < V_{f,cr}$, strain softening and a single crack characterize the post-cracking stage of FRC, because transmission length [Eq. (33a)] becomes infinitely long.
- If $V_f > V_{f,cr}$, a strain hardening behaviour can be attained in cementitious composites reinforced with long fibers. In particular, their half-length must be longer than the average crack spacing (i.e., $L_f/2 > 1.5 l_{tr}$).
- Only when the coefficient β, calculated with Eq. (30a), is far greater than 1, will all the mentioned conditions for achieving multiple cracking and strain hardening regimes be satisfied. Thus, the cohesive interface model previously described provides a single equation [Eq. (40)], which summarizes both the necessary and sufficient conditions that a fiber-reinforced composite has to satisfy in order to be classified as HPFRCC.

Eq. (40) represents a relevant outcome of the proposed model, as the existence of multiple cracking and strain hardening is the main peculiarity of HPFRCC. Although further research is needed to predict the extent of strain hardening, Eq. (40) can be effectively used to optimize the cost and the performances of FRC and to tailor more sustainable cement-based composites.

Acknowledgments

The authors wish to express their gratitude to the Italian Ministry of University and Research for financing this research work (PRIN 2006), and to Prof. Bernardino Chiaia for providing useful help.

References

[1] P.K. Mehta, P.J.M. Monteiro, Concrete — Microstructure, Properties, and Materials, McGraw-Hill, New York, 2006.
[2] Fantilli, A.P., Vallini, P., 2004. Tension stiffening range in FRC elements. In proceedings of BEFIB 2004–6th RILEM Symposium on Fibre Reinforced Concretes (FRC), Rilem Publications SARL, Bagneux.
[3] P. Balaguru, S.P. Shah, Fiber Reinforced Cement Composites, McGraw-Hill, New York, 1992.
[4] A. Hillerborg, M. Modeer, P. Peterson, Analysis of crack formation and crack growth in concrete by means of fracture mechanics and finite elements, Cem. Concr. Res. 6 (6) (1976) 773–782.
[5] B. Chiaia, A.P. Fantilli, A.P. Vallini, Evaluation of minimum reinforcement ratio in FRC members and application to tunnel linings, Mater. Struct. 40 (6) (2007) 593–604.
[6] B. Chiaia, A.P. Fantilli, A.P. Vallini, Evaluation of crack width in FRC structures and application to tunnel linings, Mater. Struct. 42 (3) (2008) 339–351.
[7] S.A.S. Akers, G.G. Garrett, Observations and predictions of fracture in asbestos–cement composites, J. Mater. Sci. 18 (7) (1983) 2209–2214.
[8] A.E. Naaman, H.W. Reinhardt, 1996. Characterization of high performance fiber reinforced cement composites–HPFRCC. In: High Performance Fiber Reinforced Cement Composites 2, E & FN Spon, London.
[9] V.C. Li, T. Kanda, Engineered cementitious composites for structural applications, ASCE J. Mater. Civ. Eng. 10 (2) (1998) 66–69.
[10] S.P. Shah, C. Ouyang, Mechanical behavior of fiber-reinforced cement-based composites, J. Am. Ceram. Soc. 74 (11) (1991) 2727–2738 2947–2953.
[11] V.C. Li, C.K.Y. Leung, Steady-state and multiple cracking of short random fiber composites, ASCE J. Eng. Mech. 118 (11) (1992) 2246–2264.
[12] V.C. Li, H.-C. Wu, Conditions for pseudo strain-hardening in fiber reinforced brittle matrix composites, Appl. Mech. Rev. 45 (8) (1992) 390–398.
[13] A.P. Fantilli, P. Vallini, A cohesive interface model for the pullout of inclined steel fibers in cementitious matrixes, J. Adv. Concr. Technol. 5 (2) (2007) 247–258.
[14] Li, V.C., Mihashi, H., Wu, H.C., Alwan, J., Brincker, R., Horii, H., Leung, C., Maalej, M., Stang, H., 1996. Micromechanical models of mechanical response of HPFRCC. In: High Performance Fiber Reinforced Cement Composites 2, E & FN Spon, London.
[15] A.E. Naaman, Engineered steel fibers with optimal properties for reinforcement of cement composites, J. Adv. Concr. Technol. 1 (3) (2003) 241–252.
[16] fib - Task Group Bond Models, 2000. Bond of reinforcement in concrete. Bulletin 10, Federation International du Beton (fib), Lausanne, Switzerland.
[17] V.C. Li, H. Stang, H. Krenchel, Micromechanics of crack bridging in fibre-reinforced concrete, Mater. Struct. 26 (8) (1993) 486–494.
[18] V.C. Li, H. Stang, H. Krenchel, Design and structural applications of stress–crack width relations in fibre reinforced concrete, Mater. Struct. 28 (4) (1995) 210–219.
[19] A.P. Fantilli, D. Ferretti, I. Iori, P. Vallini, Flexural deformability of reinforced concrete beams, ASCE J. Struct. Eng. 124 (9) (1998) 1041–1049.
[20] A.P. Fantilli, D. Ferretti, I. Iori, P. Vallini, Behaviour of R/C Elements in Bending and Tension: The Problem of Minimum Reinforcement Ratio. In Minimum Reinforcement in Concrete Members, ESIS Publication 24, Elsevier, Oxford, 1998, pp. 99–125.
[21] A.P. Fantilli, H. Mihashi, P. Vallini, Crack profile in RC, R/FRCC and R/HPFRCC members in tension, Mat. Struct. 40 (10) (2007) 1099–1114.
[22] S.T.A. Odman, Slip Between Reinforcement and Concrete, Symposium on Bond and Crack Formation in Reinforced Concrete, Tekniska Högskolans Rotaprinttryckeri, Stockholm, 1957.
[23] CEB, CEB-FIP Model Code 1990. Bulletin d'information, Thomas Telford, London, 1993, pp. 203–205.
[24] Rinaldi, Z., Grimaldi, A., 2006. Influence of high performance fiber reinforced concrete on the ductility of beam elements. In International Rilem Workshop on High performance Fiber Reinforced Cementitious Composites (HPFRCC) in Structural Applications, Rilem Publications SARL, Bagneux.
[25] V.C. Li, Engineered Cementitious Composites (ECC) —Tailored Composites Through Micromechanical Modeling. In Fiber Reinforced Concrete: Present and the Future, Canadian Society for Civil Engineering, Montreal, 1998, pp. 64–97.
[26] Kim, D. J., El-Tawil, S., Naaman, A.E., 2007. Correlation between single fiber pullout and tensile response of FRC composites with high strength steel fibers. In High Performance Fiber Reinforced Cement Composites (HPFRCC 5), Rilem Publications SARL, Bagneux.
[27] D.J. Kim, S. El-Tawil, A.E. Naaman, High Tensile Strength Strain-Hardening FRC Composites less than 2% Fiber Content, Second International Symposium on Ultra High Performance Concrete, Kassel University Press, Kassel, 2008.
[28] V.C. Li, C. Wu, S. Wang, A. Ogawa, T. Saito, Interface tailoring for strain-hardening polyvinyl alcohol-engineered cementitious composite (PVA-ECC), ACI Mater. J. 99 (5) (2002) 463–472.
[29] E.-H. Yang, S. Wang, Y. Yang, V.C. Li, Fiber-bridging constitutive law of engineered cementitious composites, J. Adv. Concr. Technol. 6 (1) (2008) 181–193.

Glossary

The following symbols are used in this paper:

A_c: Cross-sectional area of concrete (Fig. 1) or cement-based matrix (Fig. 3)
A_f: Cross-sectional area of fiber
A_s: Cross-sectional area of steel reinforcing bar
C_1, C_2: Constants of Eq. (20)
C_3: Constant of Eq. (25)
d_a: Maximum aggregate size of concrete (Fig. 1) or cement-based matrix (Fig. 3)
d_f: Diameter of fiber cross-section
E_c: Young's modulus of concrete (Fig. 1) or cement-based matrix (Fig. 3)
E_s: Young's modulus of steel reinforcing bar (Fig. 1) or fiber (Fig. 3)
f_c: Compressive strength of concrete (Fig. 1) or cement-based matrix (Fig. 3)
f_{ct}: Tensile strength of concrete (Fig. 1) or cement-based matrix (Fig. 3) with a strain-softening behaviour
f_{max}: Tensile strength of cementitious composite with a strain-hardening behaviour
f_u: Tensile strength of fiber
g: Snubbing coefficient produced by misaligned fiber [Eq. (1)]
G_{tip}: Crack tip critical energy release rate of cementitious composite [Eq. (1)]

k: Coefficient of Eq. (16b)
k_B: Bond parameter [Eq. (17)]
k_C: Cohesive parameter [Eqs. (14)–(15)]
l_{tr}: Transmission length
L: Length of RC tie
L_f: Length of fiber
N: Normal force (Fig. 1 and Fig. 3)
N_{cr}: Normal force at first cracking (Fig. 1 and Fig. 3)
N_y: Normal force at yielding of reinforcement (Fig. 1 and Fig. 3)
p_f: Perimeter of fiber cross-section
s: Slip between steel and concrete (Fig. 1) or between fiber and matrix (Fig. 3)
s_1: Slip at bond strength [Eqs. (16a)–(16b)]
s_c: Displacement of matrix cross-section (Fig. 4a)
$s_{r,m}$: Average crack spacing
s_s: Displacement of fiber cross-section (Fig. 4a)
V_f: Fiber volume fraction
$V_{f,cr}$: Critical value of fiber volume fraction
w: Crack opening displacement of concrete (Fig. 1) or cement-based matrix (Fig. 3)
w_1, w_c: Parameters of fictitious crack model (Fig. 5a) [23]
w_p: Crack opening displacement corresponding to the maximum bridging stress [Eq. (1)]
x, x_1, x_2: Dummy variables of Eqs. (29)–(31)
z: Longitudinal coordinate
ε_c: Tensile strain of concrete (Fig. 1) or cement-based matrix (Fig. 3)
$\varepsilon_{c,cr}$: Tensile strain at first cracking of concrete (Fig. 1) or cement-based matrix (Fig. 3)
ε_m: Average tensile strain of RC tie (Fig. 1)
ε_s: Tensile strain of steel reinforcing bar (Fig. 1) or fiber (Fig. 3)
ΔL: Elongation of RC tie (Fig. 1)
α: Coefficient [Eq. (19)]
β: Coefficient [Eq. (30a)]
ρ: A_s/A_c reinforcement ratio
ρ_{min}: Minimum value of reinforcement ratio
σ_c: Tensile stress of concrete (Fig. 1) or cement-based matrix (Fig. 3)
$\sigma_{c,max}$: Maximum tensile stress of matrix
σ_s: Tensile stress of steel reinforcing bar (Fig. 1) or fiber (Fig. 3)
$\sigma_{s,cr}$: Tensile stress of fiber at first cracking
τ: Bond stress
τ_{fin}: Asymptotic value of bond stress [Eqs. (16a)–(16b)]
τ_{max}: Bond strength